Feature Extraction for Computer-Aided Analysis of Mammograms

Håkan Bårman, Gösta H. Granlund and Leif Haglund

Håkan Bårman, Gösta H. Granlund and Leif Haglund, Feature Extraction for Computer-Aided Analysis of Mammograms, 1993, International journal of pattern recognition and artificial intelligence, (7), 6, 1339-1356.
http://dx.doi.org/10.1142/S0218001493000650

FEATURE EXTRACTION FOR COMPUTER-AIDED ANALYSIS OF MAMMOGRAMS

Håkan Bårman Gösta Granlund Leif Haglund
Computer Vision Laboratory, Linköping University
S-581 83 Linköping Sweden

Abstract

A framework for computer-aided analysis of mammograms is described. General computer vision algorithms are combined with application specific procedures in a hierarchical fashion. The system is under development and is currently limited to detection of a few types of suspicious areas.

The image features are extracted by using feature extraction methods where wavelet techniques are utilized. A low-pass pyramid representation of the image is convolved with a number of quadrature filters. The filter outputs are combined according to simple local Fourier domain models into parameters describing the local neighbourhood with respect to the model. This produces estimates for each pixel describing local size, orientation, Fourier phase, and shape with confidence measures associated to each parameter.

Tentative object descriptions are then extracted from the pixel-based features by application-specific procedures with knowledge of relevant structures in mammograms. The orientation, relative brightness and shape of the *object* are obtained by selection of the pixel feature estimates which best describe the object.

The list of object descriptions is examined by procedures, where each procedure corresponds to a specific type of suspicious area, e.g. clusters of microcalcifications.

Keywords: Computer vision, feature extraction, image processing, mammography, microcalcifications, wavelets.

1 Background

Breast cancer is one of the more common types of cancer. Scientific studies have shown that the mortality in breast cancer is decreased by early detection and treatment. It is well known that mammography is the best method for detection of small breast tumors. This makes it desirable to use mammography in mass screening programmes to reduce the mortality in breast cancer [1]. A mass screening program requires a large number of radiologists with special training in mammography and this involves problems such as high costs, shortage of qualified personnel, and visual fatigue.

Computer-aided analysis could be a solution to the problems mentioned above. Consequently, many efforts have been made to incorporate image processing. However, the methods developed have not been sufficient to introduce computer-aided analysis in clinical use. A survey of the area can be found in [8].

2 Overview

The digital mammogram is analyzed with a combination of general image processing and computer vision algorithms in combination with procedures which have been specially designed for the application. The following steps are carried out, where steps 1–3 are general algorithms and steps 4–6 are application specific algorithms.

1. A low-pass pyramid representation of the image is produced by low-pass filtering combined with resampling of the image.
2. Local feature extraction algorithms are used on the different layers of the low-pass pyramid to produce estimates of orientation, Fourier phase and energy.
3. The feature estimates are combined over scale, and local estimates of size (spatial frequency) are computed [11].
4. The combined phase estimates are used to guide the extraction of image objects. The phase describes the relative grey value, i.e. whether or not the pixel is darker or lighter than the surround. Brightness maxima are used as seed points for the object extraction.
5. The feature estimates of the pixels belonging to objects are used to compute parameters describing the objects. The current relatively crude implementation only includes parameters describing position, size, orientation and ‘roundness’.
6. The object list is examined by search procedures, where each procedure has knowledge of the appearance of one type of suspicious area.

Each of these steps are now described in detail.

3 The Low-Pass Pyramid

The logarithmic partitioning of the frequency domain used in wavelet theory [20] can be obtained either by scaling/translation of the filter function or by constructing a low-pass pyramid of the image. The latter alternative is preferable with respect to computational complexity. The pyramid is obtained by a low-pass filtering to eliminate the high frequencies followed by a subsampling to move the remaining spatial frequencies ‘towards’ the frequency function of the wavelet filter, e.g. a subsampling factor of two moves the spatial frequency $\pi/2$ to π. The low-pass filter should, according to the theory, be an ideal low-pass filter. Ideal low-pass filters introduce 'ringing', i.e. false edges, in the filtered images. Edges and similar structures play an important role in the later processing stages. For that reason a Gaussian filter function is used.

The current implementation has 1 octave between the layers, i.e. the subsampling factor is two. The frequency function of the Gaussian filter is given by

$$G(\mathbf{u}) = \exp(\frac{-(u_1^2 + u_2^2)}{2\sigma^2}) \tag{1}$$

and the corresponding spatial function is

$$g(\boldsymbol{\xi}) = \sqrt{2\pi}\,\sigma \exp(-(\xi_1^2 + \xi_2^2)\sigma^2/2) \tag{2}$$

with $\sigma = \pi/4$. The maximum spatial frequency [5] is normalized to π. The frequency and spatial coordinates are denoted u and ξ.

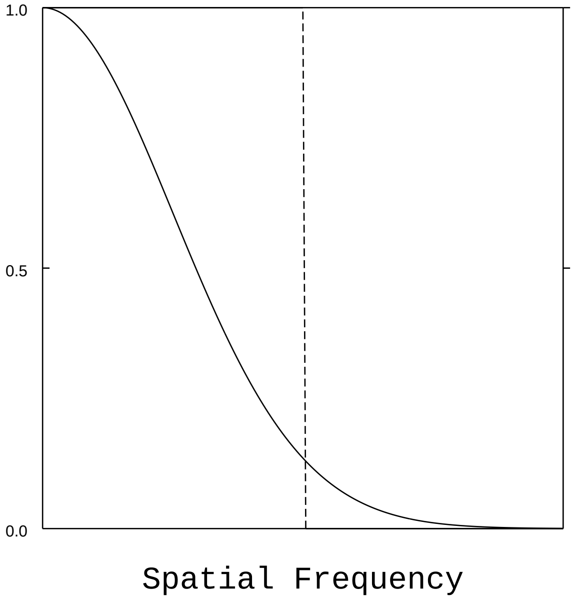

Figure 1: *The frequency function of the Gaussian filter. The dashed line indicates the ideal cutoff frequency $\pi/2$.*

This filter will not introduce any edge artifacts but will suppress the highest frequencies below $\pi/2$ and will not entirely remove frequencies above $\pi/2$ (the filter has a value of about 13.5 % of its top value at the frequency $u = \frac{\pi}{2}$). Figure 1 illustrates the difference between the ideal filter and the Gaussian filter.

Filtering and resampling is done simultaneously with an even sized filter (8×8) with its centre displaced by half a pixel unit in both ξ_1 and ξ_2, i.e. the centre is located in the middle of four pixels. The resampling is done by retaining only every other column and every other row in the filtered image. The process is schematically illustrated in Figure 2.

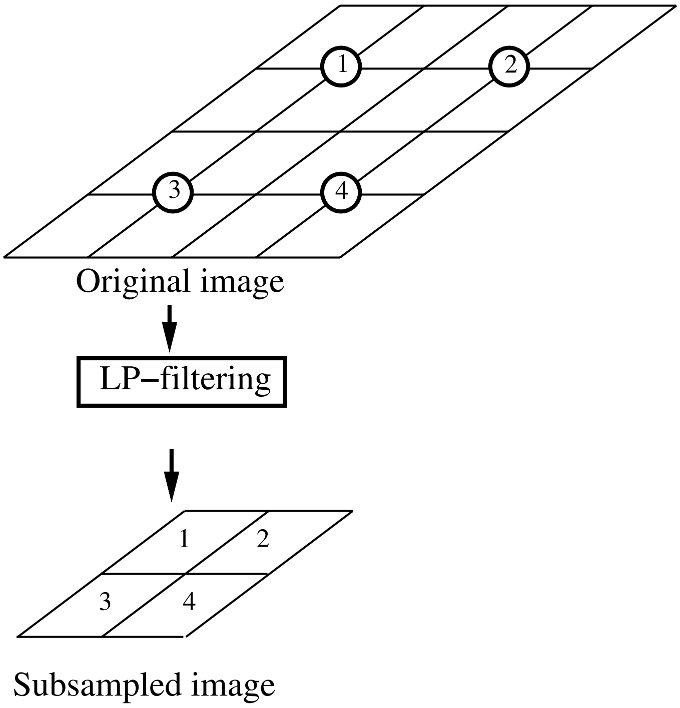

Figure 2: *Illustration of the subsampling process. The circles indicate the centre positions for the Gaussian filter. The numbers refer to the outputs from these filters.*

4 Layer Feature Extraction

The feature extraction is carried out on each of the image layers using *quadrature filters*. The quadrature filter concept forms a basis for minimizing the sensitivity to phase changes in the signal [15, 4, 11]. A number of features are obtained by combining the filter outputs according to simple local Fourier domain models. The features are local orientation, energy and phase, all estimated by convolution with four quadrature filter pairs.

The quadrature filters used are defined by polar separable frequency functions. The radial frequency function H_ρ should fulfill the wavelet requirements. The lognormal filter

$$H_\rho(\rho) = \exp(\frac{-4}{\ln 2} B^{-2} \ln^2(\rho/\rho_c)) \quad , \quad \rho \in [0 \ldots \pi]. \tag{3}$$

where ρ_c is the centre frequency and B is the 6 dB sensitivity bandwidth, is suitable if ρ_c and B have reasonable values.

Choosing $\rho_c = \pi/4$ and $B = 2$ gives:

$$H_\rho(\rho) = \exp(\frac{-1}{\ln 2} \ln^2(4\rho/\pi)) \quad , \quad \rho \in [0 \ldots \pi]. \tag{4}$$

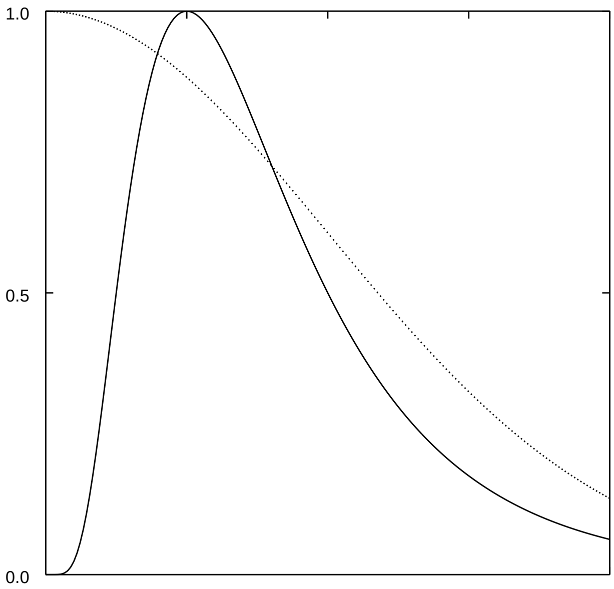

Figure 3: *The lognormal filter (solid line) given by Eq. 4 compared with the Gaussian spectrum (dashed line) obtained with the low-pass+resampling procedure.*

This choice of centre frequency places the filter in the part of the frequency spectrum where the compromise of using a Gaussian instead of an ideal low-pass filter is negligible [11] (see Figure 3). Using this filter on the subsampled images corresponds to filtering with lognormal filters with centre frequencies of $\pi/8$, $\pi/16$, $\pi/32$, …etc. Filter sets with $\rho_c = \pi/2$ and $\rho_c = \pi$ are used on the full resolution image to give additional coverage of the high spatial frequencies.

The angular frequency function specifies the orientation selectivity of the quadrature filter. Each filter set consists of four quadrature filters with the angular frequency function:

$$H_{\varphi k}(\varphi) = \cos^2(\varphi - \varphi_k) \quad , \quad \varphi_k = \pi/8,\ \ 3\pi/8,\ \ 5\pi/8,\ \ 7\pi/8 \tag{5}$$

where φ_k defines the direction of the filter.

Filters with the frequency function specified by Eq. 3 and 5 can be synthesized by:

$$H(\rho,\varphi) = a_0\, B_{00} + \sum_{n=1}^{3} a_n \left[B_{n0}\cos(n\varphi_k) + B_{n1}\sin(n\varphi_k)\right] \tag{6}$$

where the basis filters B_{ij} are defined by:

$$\begin{array}{rcll} B_{n0}(\rho,\varphi) & = & H_\rho(\rho)\,\cos(n\varphi) & n = [0\ldots 3] \\ B_{n1}(\rho,\varphi) & = & H_\rho(\rho)\,\sin(n\varphi) & n = [1\ldots 3] \end{array} \tag{7}$$

and the weight vector $\mathbf{a} = (\ a_0 \ \ a_1 \ \ a_2 \ \ a_3\ )^T$ (obtained by the theory of digital

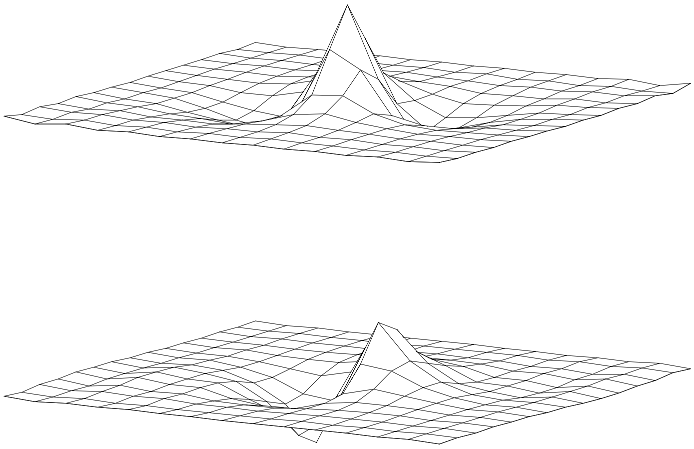

Figure 4: *One of the lognormal quadrature filters with centre frequency* $\pi/4$ *and a bandwidth of 2 octaves.*

prolate spheroidals [18, 24, 22, 23, 26]) is given by:

$$\mathbf{a} = \begin{pmatrix} 0.23675 \\ 0.39357 \\ 0.21692 \\ 0.06524 \end{pmatrix} \tag{8}$$

This approach (described in [2]) has a slight computational advantage and gives rotational invariant estimates of the local phase (Eq. 13).

The spatial representation of a quadrature filter is complex-valued with the real-valued part corresponding to a line filter and the imaginary part of the filter corresponding to an edge filter. Figure 4 contains a mesh surface plot of one the synthesized filters.

A benefit of choosing Eq. 5 as angular function is that the local orientation estimate can be estimated by the vector sum:

$$V = \sum_k q_k \exp(2\varphi_k i) \tag{9}$$

where q_k denotes the magnitude of the (complex) filter response $\mathbf{q}_k = e_k + io_k$ of the filter pair k [15]. The local orientation estimate is represented with the 'double angle' representation [10], i.e. the argument of the 2D vector V equals 2ϕ, where ϕ corresponds to the gradient direction. The magnitude of the vector is a certainty measure. The double angle representation has the advantage that it is continuous which makes local averaging a meaningful operation.

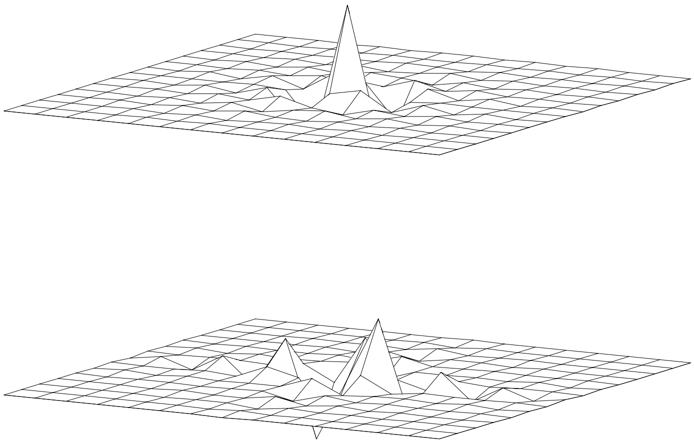

Figure 5: *'Extra' lognormal quadrature filters used on the full resolution image with a centre frequency of* π *and a bandwidth of 2 octaves.*

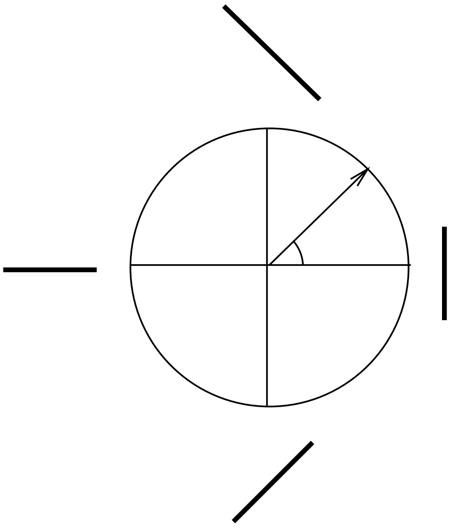

Figure 6: *The double angle representation of orientation. Taking the average of two lines, one oriented as* $\phi = 0 + \epsilon$ *and one as* $\phi = \pi - \epsilon$*, does not give the expected result if a single angle representation is used, while the double angle gives the correct answer.*

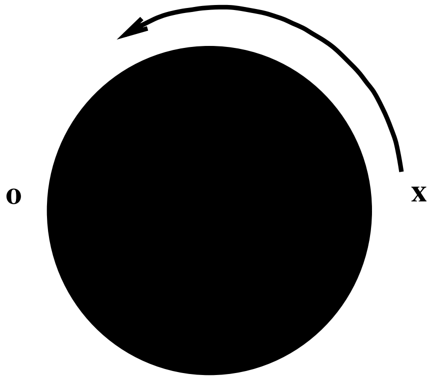

Figure 7: *Circle illustrating the edge discontinuity. The phase changes sign somewhere on the path on the edge indicated by the arrow.*

The estimation of the local energy is even simpler:

$$M = \frac{1}{2} \sum_k q_k. \tag{10}$$

This gives an estimate of the local Fourier domain energy spectrum weighted with the radial frequency function of the filter set.

The quadrature filter phase, i.e. the relation between the even and the odd filter, can be used to obtain a description of local contrast. The information resembles the information obtained by computation of local contrast or bandpass filtering, but the phase estimate gives additional information of the local image structure.

The local phase is in principle given by:

$$P = \sum_k e_k + i \sum_k o_k. \tag{11}$$

The argument of the vector P represents the local brightness with $\arg(P) \approx 0$ for lines and blobs brighter than the surroundings, $\arg(P) \approx \pi$ for lines and blobs darker than the surroundings, and $\arg(P) \approx \pi/2$ for edges. The sign cannot be determined without the orientation of the edge.

The phase sign gives problems with respect to both estimation and representation. The problem is exemplified in Figure 7. The sign of the edge can, for example, be defined as positive at '**x**' and negative at '**o**'. This implies that the phase abruptly changes its sign somewhere on the edge between the two points. A remedy is to incorporate the (edge) orientation in the phase description,

$$\mathbf{p} = \begin{pmatrix} \cos\phi \sin\theta & \sin\phi \sin\theta & \cos\theta \end{pmatrix}^T \tag{12}$$

where $\theta = \arg(P)$ and ϕ is the gradient direction. This modification of Eq. 11 makes the representation continuous, a necessary requirement for the algorithm described in the next section. Appendix A verifies that $\mathbf{p}$ can be estimated by:

$$\mathbf{p} = \sum_k \left(\frac{2a_0}{a_1} \, o_k \begin{pmatrix} \cos\varphi_k & \sin\varphi_k & 0 \end{pmatrix}^T + e_k \begin{pmatrix} 0 & 0 & 1 \end{pmatrix}^T \right). \tag{13}$$

5 Scale Feature Extraction

The estimates of orientation, energy and phase are combined over scale to find ‘events’, i.e. adjacent scale layers describing the same image structure. The algorithm handles nested objects, i.e. a pixel can contain one or more events, and is implemented as a pixelwise operation, where the feature estimates of all scales are examined with consistency measures to extract the events of the pixel. Information of the appropriate scale for description of the event and an explicit measure of the local spatial frequency is also obtained.

The implementation of the scale analysis as a pixelwise operation requires that the feature estimates of the different scale layers have identical size. This is done by resampling the layers of the feature description pyramids to the original image size. The resampling is done with a scheme very similar to the one described in section 3; nearest neighbour expansion followed by averaging with a 7 × 7 Gaussian filter specified by Eq. 2.

Note that averaging of the phase estimate would give unpredictable results if the phase estimate of Eq. 11 is used, while the representation of Eq. 13 is well-behaved. The local phase estimate (Eq. 11) is examined using an 1D-search in the scale (layer) dimension to find the number of ‘events’ described by the feature estimates of the pixel. Abrupt changes of the phase vector create new events. A scalar product is used as criterion:

$$\mathbf{p}_l \cdot \sum^{l-1} \mathbf{p}_k > \epsilon \tag{14}$$

i.e. layer l is incorporated in the event if the scalar product of the layer phase vector and the phase vector sum of the event is positive.

The dominant spatial frequency (size) of the event is estimated by:

$$F = \sum_l \delta_l M_l \exp\left(\frac{2\pi l i}{L}\right) \tag{15}$$

where L is the total number of layers, and δ_l is 1 if the layer is part of the event and 0 otherwise. The frequency estimate (the argument of the vector F) is unbiased, and the certainty measure (the magnitude of the vector F) is invariant to the frequency value in the range $[2c_b..\pi/2]$, where c_b is the centre frequency of the feature estimation filter used at the top of the low-pass pyramid [11]. Note the wraparound area in the vicinity of 2π corresponding to neighbourhoods with a mix of low and high frequencies.

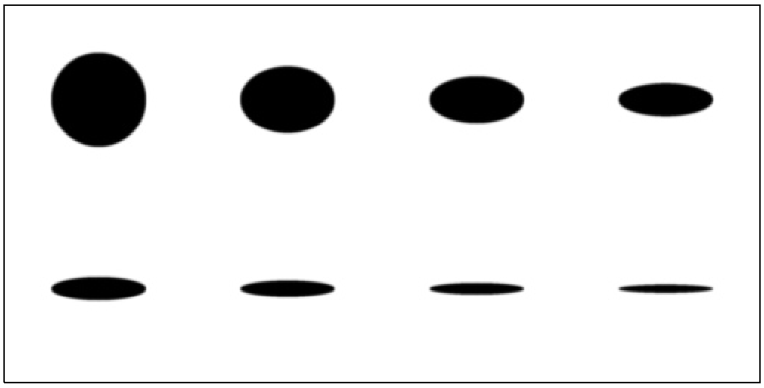

Figure 8: *Synthetic test image for evaluation of Eq. 17.*

6 Object Extraction

The extraction of image objects from the feature pyramid can be done in a number of ways, e.g. by edge contour following etc. The method used utilizes that microcalcifications are small and brighter than the surrounding tissue. It is very likely that the object extraction procedures must be extended to incorporate dectection of other types of suspicious areas.

The local phase and frequency are suitable features for selection of small and bright objects. The individual layers of the local phase pyramid are used to locate the local maxima of brightness using the maxima criterion:

$$\begin{pmatrix} 0 & 0 & 1 \end{pmatrix} \mathbf{p} > \max_{S} \begin{pmatrix} 0 & 0 & 1 \end{pmatrix} \mathbf{p}_s \tag{16}$$

where S denotes the eight adjacent pixels. Local maxima accompanied by frequency estimates indicating that the local structure is better described at another layer are disregarded. The remaining maxima are candidate objects.

The candidate object description consists of certainty (from the phase estimate), position (pixel coordinates), size (spatial frequency) and a *shape* measure computed by:

$$S = M \exp(\sqrt{1 - \mathrm{mag}(V)/M}\ \pi i). \tag{17}$$

V and M are computed by Eq. 9 and 10 on the scale layer where the brightness maximum was extracted. An argument of 0 corresponds to linear shape and π corresponds to circular shape. This measure has been used as context information in image enhancement applications [14]. Similar ideas have been used to disregard false calcification candidates originating from linear structures such as blood vessels (e.g. [17, 12]). One advantage of using Eq. 17 is that the shape estimation is done within the same feature extraction framework and no extra convolutions are required. The shape estimate has a reasonable scale invariance as indicated by Figures 8 and 9.

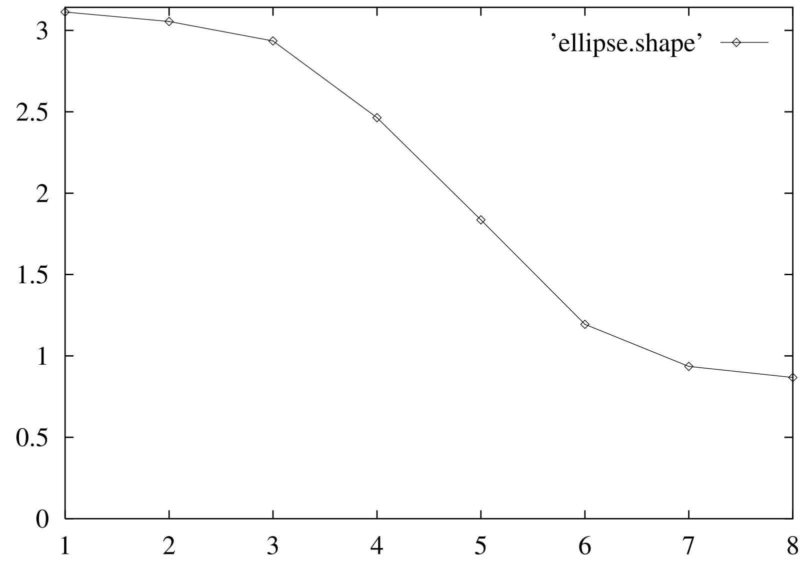

Figure 9: *The result of using Eq. 17 on Figure 8. The argument of the vector S is plotted with the estimate from the circular shape leftmost.*

7 Search Procedures

Objects with phase, frequency and shape corresponding to micro-calcifications are extracted from the object candidate list. The following steps are carried out to find clusters in the list of tentative micro-calcifications.

1. The certainty values of the tentative micro-calcifications are inserted at the object's position in an 'empty' image. The image is filtered with two filters, one Gaussian filter $a(\boldsymbol{\xi})$ and one complex-valued filter:

   $$d(\boldsymbol{\xi}) = a(\boldsymbol{\xi}) \exp(i \arg(\xi_1 + i\xi_2)) \tag{18}$$

   The quotient of the two filter outputs calculates the distance and direction to the centre of mass of the neighbourhood.

2. Local distance minima are used as seed points for cluster centres. The distances to the cluster centres are computed for all tentative micro-calcifications. A micro-calcification is assigned to the nearest cluster if the distance is shorter than a threshold R. Unassigned calcifications are removed.

3. Micro-calcifications with more than one cluster centre on shorter distance than R are used to compute 'merge-values' for pairs of clusters. The calcifications

with short distances to both cluster centres are used to compute a sum, where the contribution from an individual calcification is $c_\xi\ a(\mathbf{r}_2)$, where c_ξ is the certainty value of the calcification, $\mathbf{r}$ is the distance to the adjacent cluster and a is the Gaussian function used to specify the averaging filter in the centre of mass computation above. Two clusters are marked for merging if the sum is larger than a threshold T_m.

4. Clusters marked for merging are merged and the certainties of the cluster members are summed, $C = \sum c_\xi$. Clusters with low certainty $C < T_c$ or are disregarded. Similar relaxation approaches can be found in e.g. [7, 12].

5. The cluster centres are recomputed using

$$\mathbf{m}_c = \frac{\sum c_\xi \boldsymbol{\xi}}{\sum c_\xi} \tag{19}$$

and the shape and orientation of the cluster is measured by computation of the eigenvalues and eigenvectors of the matrix [9]

$$\frac{\sum c_\xi \boldsymbol{\xi}\boldsymbol{\xi}^T}{\sum c_\xi} - \mathbf{m}_c\mathbf{m}_c^T \tag{20}$$

8 Results

The USF database of digitised mammograms contains a number of images with malignant microcalcifications. However, the spatial resolution of the images is far from the recommended 25 μm^2/pixel [1] and the calcifications are not clearly visible on all of the images. A part of the image 'mam096' with visible calcifications is displayed in Figure 10.

The framework described in this paper is used on this image. The result from the object extraction (49 tentative calcifications) is visualized as white pixels in Figure 11. Five cluster centre candidates were found using step 1–2 described in section 7. All but four of the microcalcification candidates were assigned a cluster after the distance computation (the candidate on the top row and the three tentative calcifications at the bottom) with the threshold $R = 100$. Three of the clusters shared members and were merged into one single cluster. The smallest cluster, consisting of the three candidates at the upper right, failed to fulfill the certainty criterion of step 4. This cluster is located outside the breast area with the candidates originating from digitisation errors. The addition of a region-of-interest criterion guided by e.g. contour following of the breast contour would also eliminate the cluster [21]. The cluster centres are recomputed and the cluster shapes are estimated using Eq. 19–20. The result is superimposed on Figure 11 as black ellipses. Note that the ellipses describe the *shape and orientation* of the clusters and not the cluster border.

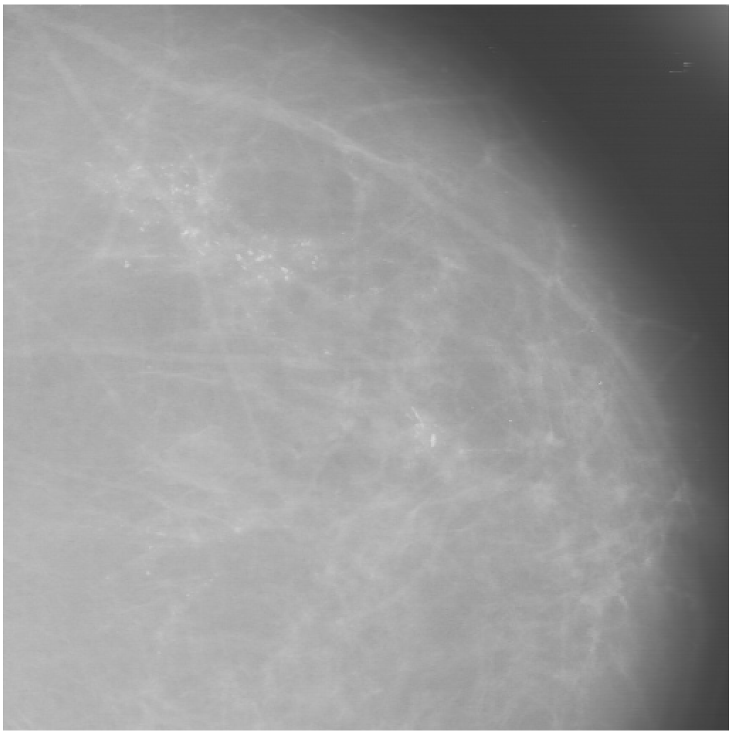

Figure 10: *A part of 'mam096' with malignant microcalcifications.*

A part of a mammogram digitised with a high resolution scanner is displayed in Figure 12. Two suspicious clusters of micro-calcifications can be found. The objects classified as tentative micro-calcifications are presented together with the cluster shapes in Figure 13.

The H. Lee Moffitt Cancer Center and Research Institute at the University of South Florida have lately uppdated the USF database with 24 mammograms digitised at 70 μm. The algorithms described in this paper were tested on seven images with clustered calcifications to get an indication of the method's performance. Box-classification with different values of the threshold parameters resulted in a sensitivity of 90.3 % (187/207). Most of the 20 undetected calcifications were faint and located within detected cluster. Most of the false alarms originated from background structure in detected clusters. One false cluster was 'created' by the classification. The total of 26 false alarms gives an accuracy of 87.8 % (187/213) in the classification.

9 Discussion

The hierarchical framework for computer-aided analysis of mammograms described in this paper consists of two parts, one part with general image processing and computer vision algorithms arranged in a wavelet inspired fashion, and one application specific part where 'objects' are extracted from the pixel-based information obtained in the

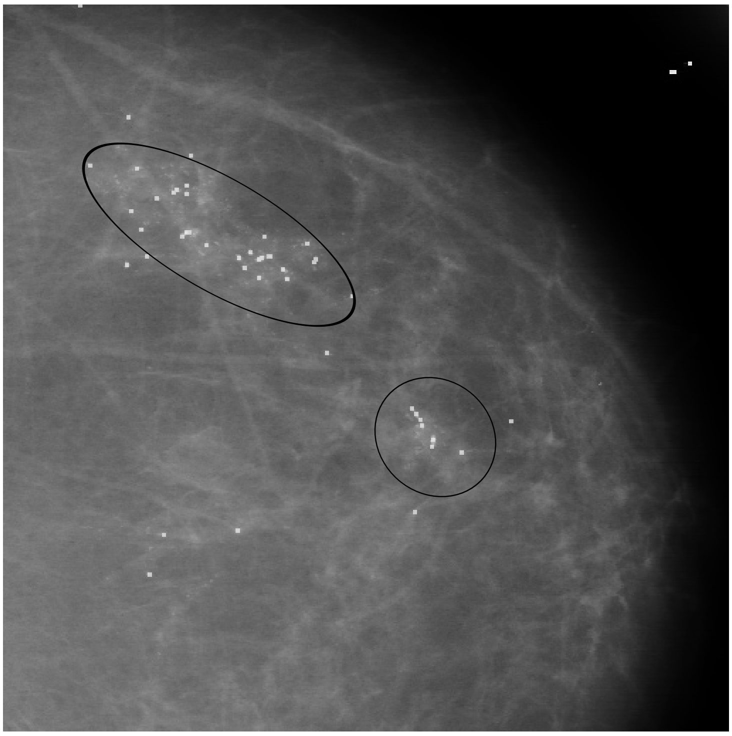

Figure 11: *The result of the calcification algorithms superimposed on the image. Tentative calcifications are white and the clusters centre, shape and orientation are represented with black ellipses.*

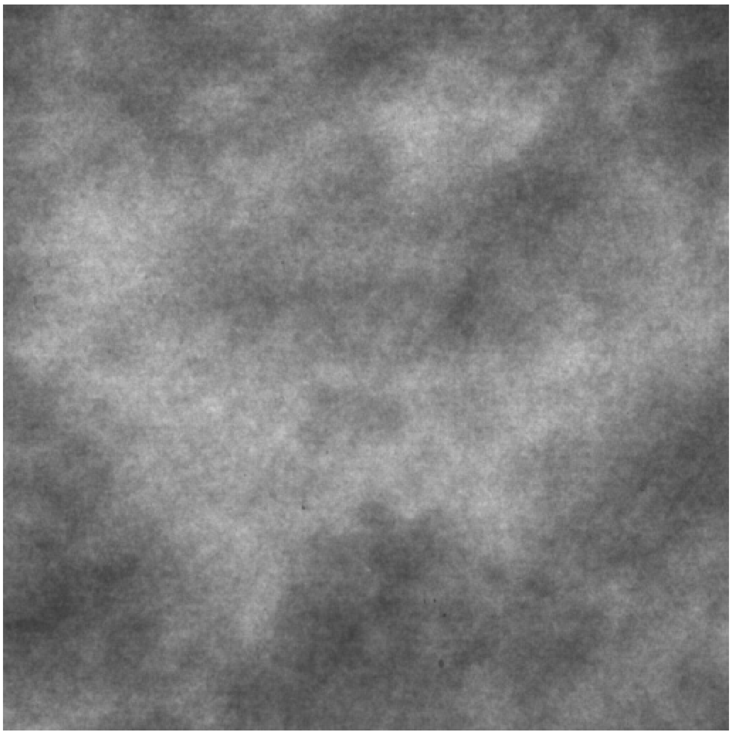

Figure 12: *Detail of high resolution mammogram with clusters of micro-calcifications*

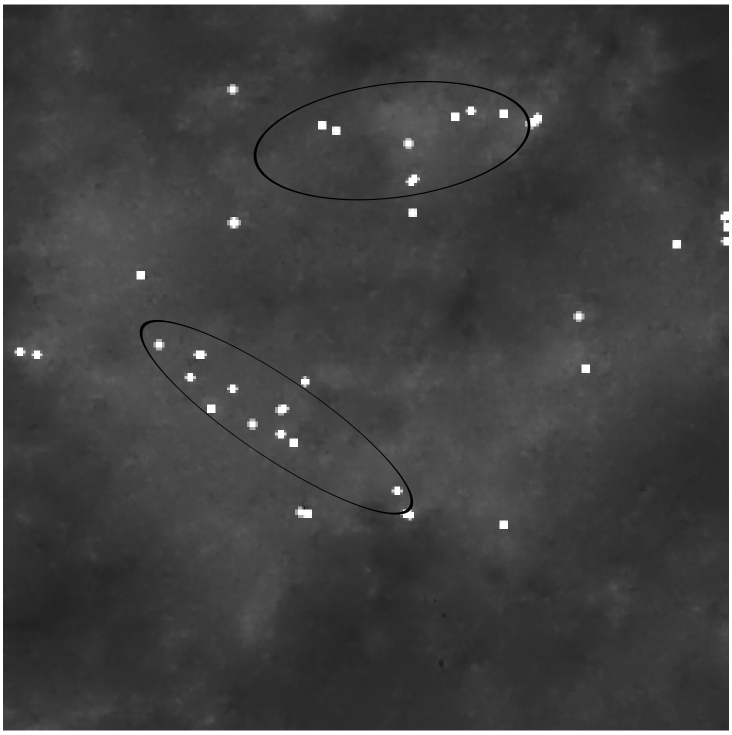

Figure 13: *The result of the calcification algorithms superimposed on the image.*

first part and specialized procedures searches for suspicious areas in the object list.

The system is currently under development and is still lacking in the domain specific features, i.e. the procedures with knowledge of the appearance of suspicious areas. New search procedures will be added, and the existing search procedures will be modified to incorporate more of the information from the feature pyramid and exchange the thresholding with more sophisticated and fully automated methods. Additions will also be made to the general image processing algorithms, e.g. hierarchical estimation of stellar patterns.

The current implementation uses a number of thresholds. Only tentative microcalcifications with certainty $c_\xi > c_T$ are included in the object list. This threshold should be set to a level close to but above the film noise. The threshold R determines whether or not a tentative calcification is part of a cluster, and is typically set to the size of the filters used in the centre of mass computation, a size that is determined from the spatial resolution of the mammogram. The thresholds for merging clusters, T_m, and disregarding clusters, T_c, are more cumbersome. Learning methods and heuristics are going to be used to automate the method.

Acknowledgement

The authors wish to thank Hans Knutsson and Mats T. Andersson at the Computer Vision Laboratory for discussions and design of some of the algorithms; Neil Roberts and Dibendu Betal at the Magnetic Resonance Research Centre, University of Liverpool, for discussions and exchange of images; Gunilla Svane and Edward Azavedo at the Department of Radiology, Karolinska Hospital, for comments on the results; and Öjvind Sundvall at MoDo Development Centre for scanning mammograms with a high resolution scanner.

Images used were provided courtesy of the University of Liverpool; Karolinska Hospital, Stockholm; the Center for Engineering and Medical Image Analysis and the H. Lee Moffitt Cancer Center and Research Institute at the University of South Florida.

This work was sponsored by NUTEK, the Swedish National Board for Industrial and Technical Development. Part of the work was carried out at the Centre for Image Analysis, Uppsala University, headed by Ewert Bengtsson.

A Proof of Eq. 13

Assume for simplicity that the quadrature filters are directed as $\varphi_0 = 0$, $\varphi_1 = \pi/4$, $\varphi_2 = \pi/2$ and $\varphi_3 = 3\pi/4$.

The even part of a quadrature filter synthesized by Eq. 6 consists of the even parts B_{00}, B_{20} and B_{21}, i.e.:

$$E_k(\rho, \varphi) = a_0\, B_{00} + a_2\, (B_{20} \cos 2\varphi_k + B_{21} \sin 2\varphi_k) \tag{21}$$

which in terms of filter responses gives:

$$e_k = a_0 b_{00} + a_2(b_{20}\cos 2\varphi_k + b_{21}\sin 2\varphi_k) \tag{22}$$

where b_{ij} is the response of the filter B_{ij}. Eq. 7 gives:

$$\begin{array}{rcl} e_0 & = & h_r(a_0 + a_2\cos 2\phi) \\ e_1 & = & h_r(a_0 + a_2\sin 2\phi) \\ e_2 & = & h_r(a_0 - a_2\cos 2\phi) \\ e_3 & = & h_r(a_0 - a_2\sin 2\phi) \end{array} \tag{23}$$

where r and ϕ are spatial coordinates. The contribution to Eq. 13 is:

$$p_3 = \sum e_k = 4a_0 h_r \tag{24}$$

The odd part of a quadrature filter synthesized by Eq. 6 consists of the odd parts B_{10}, B_{11}. B_{30} and B_{31}, i.e.:

$$O_k(\rho,\varphi) = a_1\left(B_{10}\cos\varphi_k + B_{11}\sin\varphi_k\right) + a_3\left(B_{30}\cos 3\varphi_k + B_{31}\sin 3\varphi_k\right) \tag{25}$$

which in terms of filter responses gives:

$$o_k = a_1\left(b_{10}\cos\varphi_k + b_{11}\sin\varphi_k\right) + a_3\left(b_{30}\cos 3\varphi_k + b_{31}\sin 3\varphi_k\right) \tag{26}$$

Insertion of the φ_k values gives:

$$\begin{array}{rcl} o_0 & = & h_r(a_1\cos\phi + a_3\cos 3\phi) \\ o_1 & = & h_r/\sqrt{2} \quad [a_1(\cos\phi + \sin\phi) + a_3(-\cos 3\phi + \sin 3\phi)] \\ o_2 & = & h_r(a_1\sin\phi - a_3\sin 3\phi) \\ o_3 & = & h_r/\sqrt{2} \quad [a_1(-\cos\phi + \sin\phi) + a_3(\cos 3\phi + \sin 3\phi)] \end{array} \tag{27}$$

The contribution to Eq. 13 is:

$$\begin{array}{rcl} p_1 & = & \sum \cos\varphi_k \ o_k = \dfrac{2a_0}{a_1} h_r \quad [a_1\cos\phi + a_3\cos 3\phi \\ & & +a_1/2 \quad (\cos\phi + \sin\phi) + a_3/2 \quad (-\cos 3\phi + \sin 3\phi) \\ & & +0 \\ & & -a_1/2 \quad (-\cos\phi + \sin\phi) - a_3/2 \quad (\cos 3\phi + \sin 3\phi)] \\ & = & 4a_0 h_r \ \cos\phi \end{array} \tag{28}$$

and:

$$\begin{array}{rcl} p_2 & = & \sum \sin\varphi_k \ o_k = \dfrac{2a_0}{a_1} h_r \quad [0 + \\ & & a_1/2 \quad (\cos\phi + \sin\phi) + a_3/2 \quad (-\cos 3\phi + \sin 3\phi) \\ & & +a_1\sin\phi - a_3\sin 3\phi \\ & & +a_1/2 \quad (-\cos\phi + \sin\phi) + a_3/2 \quad (\cos 3\phi + \sin 3\phi)] \\ & = & 4a_0 h_r \ \sin\phi \end{array} \tag{29}$$

This implies that $p_1 + ip_2$ is directed in the edge direction and that the even and odd parts have identical amplification ($4a_0$), viz:

$$\arg(P) = \arg(p_3 + i\sqrt{p_1^2 + p_2^2}) \tag{30}$$

References

[1] Mammografi screening. Uppföljning och kvalitetssäkring. Allmänna råd från socialstyrelsen 1990:3. Allmänna Förlaget, Kundtjänst, 106 47 Stockholm. In Swedish.

[2] M. T. Andersson. *Controllable Multidimensional Filters in Low Level Computer Vision.* PhD thesis, Linköping University, Sweden, S–581 83 Linköping, Sweden, September 1992. Dissertation No 282, ISBN 91–7870–981–4.

[3] Sue Astley, Ian Hutt, Stephen Adamson, Peter Miller, Peter Rose, Caroline Boggis, Chris Taylor, Tim Valentine, Jack Davies, and Janette Armstrong. Automation in mammography: Computer vision and human perception. In *Proc. of the 1993 SPIE Conference on Biomedical Image Processing and Biomedical Visualization.* SPIE, 1993.

[4] H. Bårman. *Hierachical Curvature Estimation in Computer Vision.* PhD thesis, Linköping University, Sweden, S–581 83 Linköping, Sweden, September 1991. Dissertation No 253, ISBN 91–7870–797–8.

[5] R. Bracewell. *The Fourier Transform and its Applications.* McGraw-Hill, 2nd edition, 1986.

[6] D. Brzakovic, P. Brzakovic, and M. Neskovic. An approach to automated screening of mammograms. In *Proc. of the 1993 SPIE Conference on Biomedical Image Processing and Biomedical Visualization.* SPIE, 1993.

[7] Heang-Ping Chan, Kunio Doi, Simranjit Galhotra, Carl J. Vyborny, Heber MacMahon, and Peter M. Jokich. Image feature analysis and computer-aided diagnosis in digital radiography. i. automated detection of microcalcifications in mammography. *Medical Physics*, 14(4):538–548, Jul/Aug 1987.

[8] Maryellen L. Giger. Computer-aided diagnosis. In A. Haus and M. J. Yaffe, editors, *Syllabus: Categorical Course in Physics. Technical Aspects of Breast Imaging*, pages 257–270. Radiological Society of North America, 1992.

[9] Rafael C. Gonzalez and Paul Wintz. *Digital Image Processing.* Addison-Wesley, second edition, 1987.

[10] G. H. Granlund. In search of a general picture processing operator. *Computer Graphics and Image Processing*, 8(2):155–178, 1978.

[11] L. Haglund. *Adaptive Multidimensional Filtering.* PhD thesis, Linköping University, Sweden, S–581 83 Linköping, Sweden, October 1992. Dissertation No 284, ISBN 91–7870–988–1.

[12] Nico Karssemeijer. Stochastic model for automated detection of calcifications in digital mammograms. *Image and Vision Computing*, 10(6):369–375, July/August 1992.

[13] Nico Karssemeijer. Recognition of clustered microcalcification using a random field model. In *Proc. of the 1993 SPIE Conference on Biomedical Image Processing and Biomedical Visualization.* SPIE, 1993.

[14] H. Knutsson, R. Wilson, and G. H. Granlund. Anisotropic non-stationary image estimation and its applications — part I: Restoration of noisy images. *IEEE Trans on Communications*, COM–31(3):388–397, March 1983. Report LiTH–ISY–I–0462, Linköping University, Sweden, 1981.

[15] Hans Knutsson. *Filtering and Reconstruction in Image Processing.* PhD thesis, Linköping University, Sweden, 1982. Diss. No. 88.

[16] Robert M. Nishikawa, Maryelllen L. Giger, Kunio Doi, Carl J. Vyborny, Robert A. Schmidt, Charles E. Mentz, Yuzheng Wu, Fang-Fung Yin, Yulei Jiang, Zhimin Huo, Ping Lu, Wei Zhang, Takihiro Ema, Ulrich Bick, John Papaioannou, and Rufus H. Nagel. Computer-aided detection and diagnosis of masses and clustered microcalcifications from digital mammograms. In *Proc. of the 1993 SPIE Conference on Biomedical Image Processing and Biomedical Visualization.* SPIE, 1993.

[17] Birger Olander. Detection of microcalcifications in mammography images using the gop-300 image processing system, 1987.

[18] A. Papoulis. *Signal Analysis.* McGraw–Hill, New York, 1977. ISBN: 0-07-048460-0.

[19] Wei Qian, Laurence P. Clarke, Maria Kallergi, Huai-Dong Li, Robert Velthuizen, Robert A. Clark, and Martin L. Silbiger. Tree-structured nonlinear filter and wavelet transform for microcalcification segmentation in mammography. In *Proc. of the 1993 SPIE Conference on Biomedical Image Processing and Biomedical Visualization.* SPIE, 1993.

[20] O. Rioul and M. Vetterli. Wavelets and signal processing. *IEEE Signal Processing Magazine*, pages 14–38, October 1991.

[21] John L. Semmlow, Annapoorin Shadagopappan, Laurens V. Ackerman, William Hand, and Frank S. Alcorn. A fully automated system for screening xeromammograms. *Computers and Biomedical Research*, 13:350–362, 1980.

[22] D. Slepian. Prolate spheroidal wavefunctions, Fourier analysis and uncertainty - IV. *Bell Syst. Tech. J.*, 43(6):3009–3058, 1964.

[23] D. Slepian. Prolate spheroidal wavefunctions, Fourier analysis and uncertainty - V, The discrete case. *Bell Syst. Tech. J.*, 57(5):1371–1430, 1978.

[24] D. Slepian and H. O. Pollak. Prolate spheroidal wavefunctions, Fourier analysis and uncertainty - I. *Bell Syst. Tech. J.*, 40(1):43–64, 1961.

[25] Wolfgang Spiesberger. Mammogram inspection by computer. *IEEE Transactions on Biomedical Engineering*, BME-26(4), April 1979.

[26] R. Wilson. Finite prolate spheroidal sequences and their applications i: generation and properties. *IEEE Trans. on Pattern Analysis and Machine Intelligence*, PAMI-9(6):787–795, Nov. 1987.

[27] Kevin S. Woods, Jeffrey L. Solka, Carey E. Priebe, Christopher C. Doss, Kevin W. Bowyer, and Laurence P. Clarke. Comparative evaluation of pattern recognition techniques for detection of microcalcifications. In *Proc. of the 1993 SPIE Conference on Biomedical Image Processing and Biomedical Visualization.* SPIE, 1993.